

Efficient second-order semi-implicit finite element method for fourth-order nonlinear diffusion equations

Sana Keita^a, Abdelaziz Beljadid^{a,b,*}, Yves Bourgault^b

^a*International Water Research Institute, Mohammed VI Polytechnic University, Morocco*

^b*Department of Mathematics and Statistics, University of Ottawa, Canada*

Abstract

We focus here on a class of fourth-order parabolic equations that can be written as a system of second-order equations by introducing an auxiliary variable. We design a novel second-order fully discrete mixed finite element method to approximate these equations. In our approach, we propose new techniques using the second-order backward differentiation formula for the time derivative and a special technique for the approximation of nonlinear terms. The use of the proposed technique for nonlinear terms makes the developed numerical scheme efficient in terms of computational cost since the proposed method only deals with a linear system at each time step and no iterative resolution is needed. A numerical convergence study is performed using the method of manufactured and analytical solutions of the system where we investigate different boundary conditions. With respect to the spatial discretization, convergence rates are found to at least match a priori error estimates available for linear problems. The convergence analysis is completed with an investigation of the temporal discretization where we numerically demonstrate the second-order time-accuracy of the proposed scheme using the method of reference solution. We present a series of numerical tests to demonstrate the efficiency and robustness of the proposed scheme.

Keywords: Second-order scheme, Numerical convergence analysis, Mixed finite element, Fourth-order equation, Diffuse-interface model, Cahn-Hilliard equation

1. Introduction

High order partial differential equations (PDEs) containing the bi-harmonic operator often arise in two-phase and multiphase problems from fluid mechanics and solid mechanics. Examples in the literature include the thin film equations [21, 29, 34, 35, 42], the Cahn-Hilliard (CH) equations [11, 12], ocean and atmosphere circulation models [18], tumor-growth models [13, 49], cancer modeling [40], biological entities [25, 39], image processing [7], the fourth-order model for the approximation of crack propagation [1], models of unstable infiltration through porous media [5, 14], etc.

*Corresponding author.

Email addresses: sana.keita@um6p.ma (Sana Keita), abdelaziz.beljadid@um6p.ma (Abdelaziz Beljadid), ybourg@uottawa.ca (Yves Bourgault)

Nonlinearity and discretization of high-order spatial operators (fourth-order) are the main issues encountered when numerically solving these equations. The nonlinearity is often induced by non-constant mobility and nonlinear free energy functions. As a result, several different procedures have been employed over the years to deal with higher-order equations, for instance, mixed formulations, where the governing equations are split into a coupled system of lower-order differential equations [9, 23].

There have been many studies on numerical methods for solving parabolic equations involving the bi-harmonic operator, including finite difference [8, 47, 55], finite volume [16, 30], Fourier spectral [32, 53] and finite element methods [3, 10, 20, 36]. Most studies using finite element method focus on mixed formulation to approximate the CH equations [2, 4, 19, 28, 37, 38, 54], see also the references therein. Second-order time-accurate methods for the CH equations have mostly been studied for variants of the Crank-Nicolson scheme with various treatment of the nonlinear energy term [31, 44, 48, 51]. Convex-concave splitting of the energy term is often employed, but it leads to nonlinear schemes except for some particular forms of the energy function. Addition of stabilization terms, use of Hermite quadrature formula and/or explicit treatment or extrapolation of the energy function, although leading to a linear scheme, is very limited in term of stability constraint [31, 46]. Recently, Yang et al. [52] proposed a family of second-order unconditionally energy-stable schemes for CH equations by reformulating the equations into an equivalent system employing a scalar auxiliary variable, giving rise to four equations to solve at each time step.

In the current study, we focus on the numerical approximation of the CH equations. We propose a novel linear semi-implicit time stepping scheme to approximate the problem. The proposed scheme maintains second-order accuracy in time by using second-order backward difference formula (BDF2) for the time derivative, extrapolation formula for the non-constant mobility function and a special technique using semi-implicit Taylor approximation for the nonlinear energy function. The use of Taylor expansion on a term in solving partial differential equations was introduced by Rosenbrock [45]. A scheme employing the Crank-Nicolson time integration and Taylor series expansions of the nonlinear terms were proposed by Vignal et al. [48] for general classes of phase-field models with polynomial potentials. Their resulting system is nonlinear and therefore, requires an iterative method for the linearization. Our scheme applies to general classes of phase-field models with any form of free energy function of class \mathcal{C}^2 and does not require an iterative method. A linear system is solved at each time step. We perform numerical convergence analysis in space using both a manufactured and analytical solutions to demonstrate optimal convergence rates of the L^2 - and H^1 -error norms using standard Lagrange elements. Better, super-convergence of the L^2 -error norm is observed with quadratic Lagrange elements. Numerical results from selected test cases also show that the proposed scheme is efficient in terms of computational cost and satisfies the free energy dissipation and the mass conservation properties.

The outline of the paper is as follows. In section 2, the model equation is introduced and its main mathematical properties are briefly discussed. In section 3, the fully discrete finite element approximation scheme is presented. In Section 4, the spatial convergence rates, accuracy and robustness of the proposed scheme are numerically investigated by means of several numerical test cases. Second-order time-accuracy is verified with both constant and variable mobility function, and the discrete energy dissipation and the discrete mass conservation properties of the scheme are illustrated. Section 5 provides a summary and some concluding remarks.

2. Model equation

Let $\Omega \subset \mathbb{R}^d$, where $d = 2$ or 3 , be an open bounded set with sufficiently smooth boundary $\partial\Omega$, and $T > 0$ a fixed positive time. We focus on a class of fourth-order parabolic PDEs of the form

$$\partial_t u = -\gamma \nabla \cdot (f(u) \nabla \Delta u) + \nabla \cdot (f(u) \nabla \varphi'(u)) \quad \text{in } \Omega \times (0, T), \quad (2.1)$$

with unknown $u : \Omega \times [0, T] \rightarrow \mathbb{R}$, the given functions $f : \mathbb{R} \rightarrow \mathbb{R}_{\geq 0}$, $\varphi : \mathbb{R} \rightarrow \mathbb{R}$ are smooth, and $\gamma \in \mathbb{R}_{\geq 0}$ is a constant. Depending on the applications, u can describe the height of a liquid phase spreading on a solid surface [29, 34], the concentration, volume fraction or density of a phase in a mixture [11, 12], etc.

By introducing an auxiliary unknown w , the fourth-order equation (2.1) can be written in the following system of second-order equations

$$\begin{aligned} \partial_t u &= \nabla \cdot (f(u) \nabla w) \quad \text{in } \Omega \times (0, T), \\ w &= -\gamma \Delta u + \varphi'(u) \quad \text{in } \Omega \times (0, T). \end{aligned} \quad (2.2)$$

System (2.2) is to be supplemented by the initial condition

$$u(\mathbf{x}, 0) = u_0(\mathbf{x}) \quad \text{in } \Omega, \quad (2.3)$$

and the no-flux boundary conditions

$$\nabla u \cdot \mathbf{n} = \nabla w \cdot \mathbf{n} = 0 \quad \text{on } \partial\Omega \times (0, T), \quad (2.4)$$

where \mathbf{n} is the exterior unit normal vector to $\partial\Omega$.

There are two important properties for the equations (2.2) with the natural boundary conditions (2.4). The first one is the conservation of mass. In fact,

$$\frac{d}{dt} \int_{\Omega} u \, d\mathbf{x} = \int_{\Omega} \partial_t u \, d\mathbf{x} = \int_{\Omega} \nabla \cdot (f(u) \nabla w) \, d\mathbf{x} = \int_{\partial\Omega} f(u) \nabla w \cdot \mathbf{n} \, d\mathbf{x} = 0, \quad (2.5)$$

that is the total amount of the phase in the domain must always be equal to the given initial amount of this phase. The equation is associated with the total free energy functional

$$J(u) = \int_{\Omega} \left(\frac{\gamma}{2} |\nabla u|^2 + \varphi(u) \right) d\mathbf{x}, \quad (2.6)$$

which satisfies the total free energy dissipation, that is

$$\frac{dJ}{dt} = \int_{\Omega} (\gamma \nabla u \nabla \partial_t u + \varphi'(u) \partial_t u) \, d\mathbf{x} = \int_{\Omega} w \partial_t u \, d\mathbf{x} = - \int_{\Omega} f(u) |\nabla w|^2 \, d\mathbf{x} \leq 0. \quad (2.7)$$

A weak formulation of problem (2.1) can be obtained by multiplying (2.1) by test function v . Integrating by parts and using the boundary conditions (2.4) eventually lead to: Find $u \in H^2(\Omega)$ such that

$$\int_{\Omega} \partial_t u v \, d\mathbf{x} + \int_{\Omega} \gamma f(u) \Delta u \Delta v \, d\mathbf{x} + \int_{\Omega} \gamma \Delta u \nabla f(u) \cdot \nabla v \, d\mathbf{x} + \int_{\Omega} f(u) \nabla \varphi'(u) \cdot \nabla v \, d\mathbf{x} = 0, \quad (2.8)$$

for all $v \in H^2(\Omega)$. A weak formulation for problem (2.2) can be obtained by multiplying the first and second equation in (2.2) by test functions v and q , respectively: Find $(u, w) \in H^1(\Omega) \times H^1(\Omega)$ such that

$$\begin{aligned} \int_{\Omega} u_t v \, d\mathbf{x} + \int_{\Omega} f(u) \nabla w \cdot \nabla v \, d\mathbf{x} &= 0, \quad \forall v \in H^1(\Omega), \\ \int_{\Omega} w q \, d\mathbf{x} - \int_{\Omega} \gamma \nabla u \cdot \nabla q \, d\mathbf{x} - \int_{\Omega} \varphi'(u) q \, d\mathbf{x} &= 0, \quad \forall q \in H^1(\Omega). \end{aligned} \quad (2.9)$$

Theoretical results on the existence of solutions to (2.1) and (2.2) in the sense (2.8) and (2.9), respectively, can be found in [15, 22, 24].

3. Numerical methods

3.1. Spatial discretization

Kästner et al. [38] showed that the convergence rates for approximations that are less than second-order in space are suboptimal when using the direct weak formulation (2.8). This is due to the discretization of higher-order differential operators. The weak formulation (2.9) naturally leads to mixed finite element methods which provide robust numerical approaches to compute solutions of high-order PDEs by avoiding the discretization of high-order derivatives [9, 23]. In the following, we will use the mixed weak formulation (2.9).

We discretize in space by continuous piecewise Lagrange finite elements. Given a polygonal domain Ω , we consider \mathcal{T}_h being a uniform partitioning of the domain Ω into disjoint triangles κ , so that

$$\overline{\Omega} = \bigcup_{\kappa \in \mathcal{T}_h} \kappa. \quad (3.1)$$

The element mesh size h is defined as

$$h := \max_{\kappa \in \mathcal{T}_h} h_{\kappa}, \quad (3.2)$$

where $h_{\kappa} := \text{diam}(\kappa)$. Associated with the partitioning \mathcal{T}_h is the finite element space

$$\mathcal{V}_h = \left\{ v_h \in \mathcal{C}^0(\overline{\Omega}, \mathbb{R}) : v_h|_{\kappa} \in \mathbb{P}_k, \quad \forall \kappa \in \mathcal{T}_h \right\} \subset H^1(\Omega), \quad (3.3)$$

where \mathbb{P}_k denotes the space of polynomials of degree less than or equal to k on any element κ .

The resulting semi-discrete (in space) weak formulation of problem (2.2)-(2.4) is given as follows: Find $(u_h, w_h) \in \mathcal{C}^1(0, T; \mathcal{V}_h \times \mathcal{V}_h)$ such that, for all $t \in [0, T]$,

$$\begin{aligned} \int_{\Omega} \partial_t u_h(t) v_h \, d\mathbf{x} + \int_{\Omega} f(u_h(t)) \nabla w_h(t) \cdot \nabla v_h \, d\mathbf{x} &= 0, \quad \forall v_h \in \mathcal{V}_h, \\ \int_{\Omega} w_h(t) q_h \, d\mathbf{x} - \int_{\Omega} \gamma \nabla u_h(t) \cdot \nabla q_h \, d\mathbf{x} - \int_{\Omega} \varphi'(u_h(t)) q_h \, d\mathbf{x} &= 0, \quad \forall q_h \in \mathcal{V}_h, \\ u_h(0) &= \Pi_h u_0, \end{aligned} \quad (3.4)$$

where Π_h is an interpolation or projection operator on \mathcal{V}_h .

3.2. Temporal discretization

The time interval $[0, T]$ is discretized as

$$t_n = n\Delta t, \quad n = 0, 1, \dots, N, \quad \Delta t = \frac{T}{N}, \quad (3.5)$$

where Δt is the time step used. We consider a uniform discretization in time by a semi-implicit stepping method, so that $u_h^n \simeq u_h(t_n)$ for $n = 0, 1, \dots, N$. For the temporal discretization of the equations (2.2), all linear terms are approximated implicitly. The time derivative $\partial_t u_h$ is approximated using a second-order backward differentiation formula (BDF2). To allow for a linear scheme, a second-order extrapolation formula is employed for the mobility function $f(u_h)$ while the energy term $\varphi'(u_h)$ is evaluated using the Taylor approximation of second-order truncation error. We have noticed from numerical experiments that the approximation of the nonlinear energy term using the proposed technique is better than by an extrapolation which leads to severe stability constraint. Our technique introduces a linear implicit term which improves the stability constraint. We emphasize two main benefits resulting from the proposed scheme. First of all, it is easy to implement. No fixed point iteration for solving the system is required. Only one linear system needs to be solved at every time step. The proposed scheme is written as follows: given a suitable approximation of the initial solution $u_h^{-1} = \Pi_h u_0 \in \mathcal{V}_h$ and a proper initialization for $u_h^0 \in \mathcal{V}_h$, find $(u_h^n, w_h^n) \in \mathcal{V}_h \times \mathcal{V}_h$ such that

$$\begin{aligned} \int_{\Omega} \left(\frac{3u_h^n - 4u_h^{n-1} + u_h^{n-2}}{2\Delta t} \right) v_h d\mathbf{x} + \int_{\Omega} (2f(u_h^{n-1}) - f(u_h^{n-2})) \nabla w_h^n \cdot \nabla v_h d\mathbf{x} &= 0, \quad \forall v_h \in \mathcal{V}_h, \\ \int_{\Omega} w_h^n q_h d\mathbf{x} - \int_{\Omega} \gamma \nabla u_h^n \cdot \nabla q_h d\mathbf{x} - \int_{\Omega} (\varphi'(u_h^{n-1}) + \varphi''(u_h^{n-1})(u_h^n - u_h^{n-1})) q_h d\mathbf{x} &= 0, \quad \forall q_h \in \mathcal{V}_h, \end{aligned} \quad (3.6)$$

for all $1 \leq n \leq N$.

The numerical algorithm (3.6) is a two steps scheme and therefore, it requires the use of a starting procedure to obtain u_h^0 . Here, we use a semi-implicit backward Euler method

$$\begin{aligned} \int_{\Omega} \left(\frac{u_h^0 - u_h^{-1}}{\Delta t} \right) v_h d\mathbf{x} + \int_{\Omega} f(u_h^{-1}) \nabla w_h^0 \cdot \nabla v_h d\mathbf{x} &= 0, \quad \forall v_h \in \mathcal{V}_h, \\ \int_{\Omega} w_h^0 q_h d\mathbf{x} - \int_{\Omega} \gamma \nabla u_h^0 \cdot \nabla q_h d\mathbf{x} - \int_{\Omega} \varphi'(u_h^{-1}) q_h d\mathbf{x} &= 0, \quad \forall q_h \in \mathcal{V}_h, \end{aligned} \quad (3.7)$$

to compute u_h^0 starting from u_h^{-1} .

The numerical treatment of the energy term $\varphi'(u_h)$ uses the following semi-implicit Taylor expansion of $\varphi'(u_h(t_n))$ about $u_h = u_h(t_{n-1})$:

$$\varphi'(u_h(t_{n-1})) + \varphi''(u_h(t_{n-1}))(u_h(t_n) - u_h(t_{n-1})) = \varphi'(u_h(t_n)) - \frac{1}{2}(u(t_n) - u(t_{n-1}))^2 \varphi^{(3)}(\bar{u}^n), \quad (3.8)$$

where \bar{u}^n is between $u_h(t_{n-1})$ and $u_h(t_n)$. To evaluate the local truncation error

$$\tau^n(q_h) = \int_{\Omega} -\frac{1}{2}(u(t_n) - u(t_{n-1}))^2 \varphi^{(3)}(\bar{u}^n) q_h d\mathbf{x} \quad (3.9)$$

of the energy term, one expands again $u_h(t_{n-1})$ in (3.9) around the point $t = t_n$ and gets

$$\tau^n(q_h) = -\frac{\Delta t^2}{2} \int_{\Omega} (\partial_t u_h(\xi^n))^2 \varphi^{(3)}(\bar{u}^n) q_h d\mathbf{x}, \quad (3.10)$$

where $\xi^n = \xi^n(\mathbf{x}) \in [t_{n-1}, t_n]$ for all $\mathbf{x} \in \Omega$. The backward differentiation formula used for the numerical treatment of $\partial_t u_h$ is known to have error that is second-order in time and one can easily show that the extrapolation technique used for the approximation of the mobility term $f(u_h)$ has an order of accuracy of $\mathcal{O}(\Delta t^2)$. Hence, the scheme (3.6) is second-order accurate in time.

3.3. Solution of the discrete system

Equations in (3.6) or (3.7) consist in a coupled linear system in u_h^n and w_h^n of the following form

$$\begin{bmatrix} M_1 & A_1 \\ -A_2 & M_2 \end{bmatrix} \begin{bmatrix} U \\ W \end{bmatrix} = \begin{bmatrix} F \\ G \end{bmatrix}, \quad (3.11)$$

where M_i and A_i , $i = 1, 2$, are mass and stiffness matrices, respectively; U and W correspond to the finite element degrees of freedom for u_h^n and w_h^n , respectively; F and G are properly chosen constant vectors.

This linear system shares characteristics with those for saddle point problems, such as the block-structured sparsity pattern, the lack of positive definiteness, etc. These linear systems are difficult to solve. The use of a direct solver may lead to a lot of fill-in, while iterative solvers may be impacted by the indefiniteness of the matrix. For our 2D test cases, we used the sparse linear solver UMFPACK [17], which mitigates the fill-in and provides a relatively efficient solution. However, for 3D computations, one would need to use iterative methods. One may attempt to build a dedicated iterative method accounting for the fact that all the blocks M_i and A_i are at least semi-positive definite, a property usually not shared by general saddle point problems.

3.4. Mass conservation

As usual in finite element methods with no-flux boundary conditions, the scheme (3.6) is conservative. In fact, taking $v_h = 1$ in the first equation of (3.6) and (3.7), respectively, leads to

$$\int_{\Omega} \frac{3u_h^n - 4u_h^{n-1} + u_h^{n-2}}{2\Delta t} d\mathbf{x} = 0 \quad \text{and} \quad \int_{\Omega} \frac{u_h^0 - u_h^{-1}}{\Delta t} d\mathbf{x} = 0. \quad (3.12)$$

It follows by induction from (3.12) that

$$\int_{\Omega} u_h^n d\mathbf{x} = \int_{\Omega} u_h^0 d\mathbf{x}, \quad \forall n = 1, \dots, N, \quad (3.13)$$

which means that the discrete total mass is conserved over time.

4. Numerical results

A series of numerical problems in two dimensions is given in this section to test the performance of the numerical method developed in section 3. All the algorithms for the simulations are implemented using FreeFem++ software [33].

4.1. Numerical results — Convergence

In this subsection we numerically show the rates of convergence in space and time of the algorithm (3.6)-(3.7). We first conduct a detailed investigation using the method of manufactured solution for a constant mobility function. We then use an analytic solution for a non-constant mobility function to perform a similar error analysis.

4.1.1. Manufactured solution

Following the framework presented in [37, 38, 52, 54], we employ a manufactured solution to test our method. The idea is to use an arbitrary regular function as analytic solution for the computation of numerical errors.

Substituting in (2.2) the function

$$\hat{u} = (t + 1) \sin(\alpha\pi x), \quad (4.1)$$

where $\alpha \in \mathbb{R}$, by assuming a free energy function

$$\varphi(u) = \frac{u^4}{4} - \frac{u^2}{2}, \quad (4.2)$$

and a constant mobility function $f(u) = 1$, yields

$$\begin{cases} \hat{u}_t = \nabla \cdot (\nabla \hat{w}) + S, \\ \hat{w} = -\gamma \Delta \hat{u} + \varphi'(\hat{u}), \end{cases} \quad (4.3)$$

where the residual S is given by

$$\begin{aligned} S = & \sin(\alpha\pi x) + 3(t + 1)^3 \alpha^2 \pi^2 \sin^3(\alpha\pi x) + \gamma(t + 1) \alpha^4 \pi^4 \sin(\alpha\pi x) - (t + 1) \alpha^2 \pi^2 \sin(\alpha\pi x) \\ & - 6(t + 1)^3 \alpha^2 \pi^2 \sin(\alpha\pi x) \cos^2(\alpha\pi x) \end{aligned} \quad (4.4)$$

and the auxiliary variable \hat{w} is given by

$$\hat{w} = \gamma(t + 1) \alpha^2 \pi^2 \sin(\alpha\pi x) + (t + 1)^3 \sin^3(\alpha\pi x) - (t + 1) \sin(\alpha\pi x). \quad (4.5)$$

We assumed here a constant mobility function $f(u) \equiv 1$ to simplify the calculation of the residual function S , but the energy term (4.2) is a nonlinear non-zero function. This will allow to test the impact of the new proposed technique for the discretization of the nonlinear energy term, based on a semi-implicit Taylor expansion of the latter.

For the convergence analysis in space, we compute the L^2 - and H^1 -error norms on the discrete solution \hat{u}_h of (4.3) at the final time, which are defined as

$$\begin{aligned} \|\hat{u} - \hat{u}_h\|_{L^2(\Omega)} &= \left(\int_{\Omega} |\hat{u} - \hat{u}_h|^2 d\mathbf{x} \right)^{1/2}, \\ \|\hat{u} - \hat{u}_h\|_{H^1(\Omega)} &= \left(\int_{\Omega} \left(|\hat{u} - \hat{u}_h|^2 + |\nabla(\hat{u} - \hat{u}_h)|^2 \right) d\mathbf{x} \right)^{1/2}. \end{aligned} \quad (4.6)$$

A set of boundary conditions for the system has to be imposed. We will investigate both Dirichlet and non-homogeneous Neumann boundary conditions using the exact solution (4.1) and (4.5) at

boundaries. The linear (\mathbb{P}_1) and quadratic (\mathbb{P}_2) Lagrange finite element discretizations and four uniform meshes (25×25 , 50×50 , 100×100 and 200×200 elements) of the unit square (centered at the origin) domain have been considered. We use a fixed time step $\Delta t = 10^{-5}$ and consider a small value for the parameter $\gamma = 10^{-4}$. The final computational time is $T = 10^{-3}$.

We first impose Dirichlet conditions $\hat{u}_h = \Pi_h \hat{u}$ and $\hat{w}_h = \Pi_h \hat{w}$ on boundaries. The numerical errors on \hat{u}_h are computed for different values of the parameter α . Figure 1 shows these errors as a function of the element size h . Optimal convergence rates, i.e. $\mathcal{O}(h^{k+1})$ and $\mathcal{O}(h^k)$, are obtained for the L^2 - and H^1 -error, respectively. Better, we get super convergence for the L^2 -norm error with the quadratic Lagrange elements. The error increases with α , which controls the gradient of the solution. However, the rates of convergence remain the same, and therefore, are independent from the choice of α .

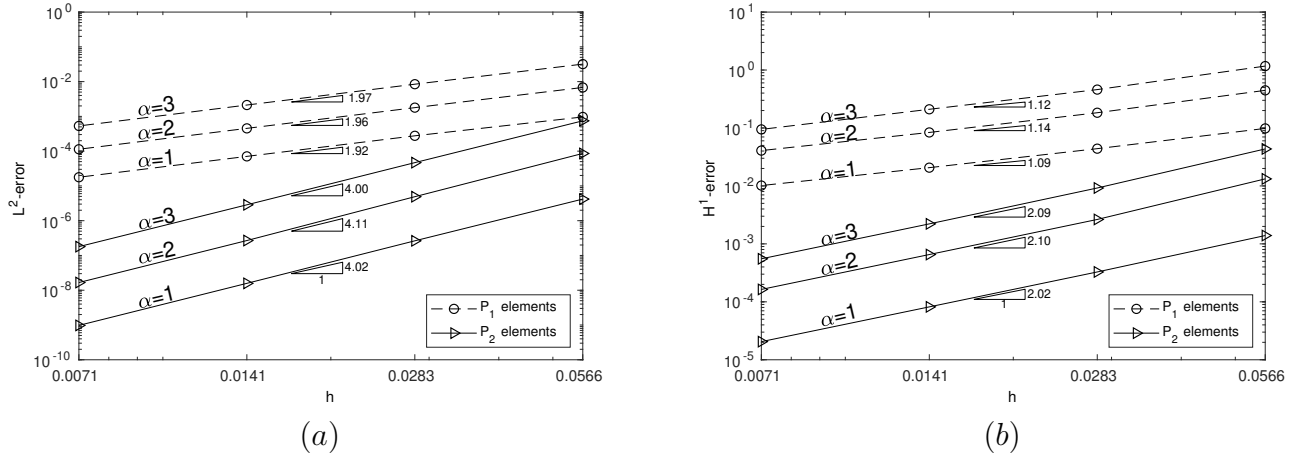


Figure 1: Error and convergence rates of linear and quadratic Lagrange elements: (a) L^2 -error, and (b) H^1 -error on the discrete solution \hat{u}_h as function of the element size h . Results are obtained with Dirichlet boundary conditions.

We next impose non-homogeneous Neumann conditions $\frac{\partial \hat{u}_h}{\partial \mathbf{n}} = \Pi_h \frac{\partial \hat{u}}{\partial \mathbf{n}}$ and $\frac{\partial \hat{w}_h}{\partial \mathbf{n}} = \Pi_h \frac{\partial \hat{w}}{\partial \mathbf{n}}$. Here, also optimal convergence rates in the L^2 - and H^1 -error are obtained. Again, super-convergence in the L^2 -norm is observed with quadratic Lagrange elements. To facilitate comparison between the results obtained using Dirichlet and Neumann conditions, the errors computed for $\alpha = 2$ are shown in Figure 2. We can see that the L^2 -error with Neumann conditions are larger than with Dirichlet conditions, but the H^1 -error are almost identical.

We have performed a similar error analysis with the L^2 - and H^1 -error on the auxiliary variable \hat{w}_h and found the same orders of convergence as for \hat{u}_h . However, the H^1 -error on w_h is larger and the order of magnitude of the difference increases with α . This is natural since $\hat{w}_h = -\gamma \Delta \hat{u}_h + \varphi'(\hat{u}_h)$ is more difficult to approximate and the gradient of the solution increases with α more rapidly than for \hat{u}_h .

To test the temporal convergence rate, we compute a reference solution $(u_h^{\text{ref}}, w_h^{\text{ref}})$ on a grid of 50×50 elements using a very small time step $\Delta t = 10^{-8}$ at the final time $T = 10^{-3}$. We choose the quadratic Lagrange element and impose Dirichlet boundary conditions to minimize the spatial error. Moreover, with quadratic elements, fixed computational time and time step give smaller error than with \mathbb{P}_1 elements (see Table 1 in section 4.1.2). We analyze the numerical convergence

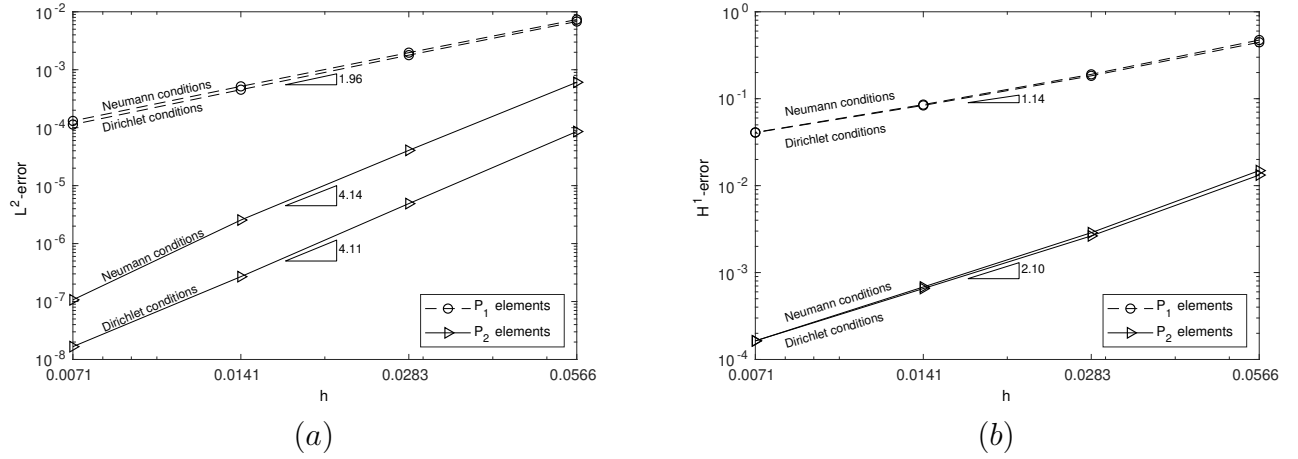


Figure 2: Quantitative comparison of the error computed with Dirichlet and Neumann boundary conditions, respectively: (a) L^2 -error, and (b) H^1 -error on the discrete solution \hat{u}_h as function of the element size h .

in time by varying the time step Δt systematically between 0.125×10^{-4} and 2×10^{-4} . For each time step, the numerical errors in the L^2 - and L^∞ -norms are computed. Figure 3 shows the L^2 - and L^∞ -error on \hat{u}_h and \hat{w}_h , respectively, and the order of convergence of the numerical solution with respect to the reference solution. We obtain almost a second-order convergence rate in time.

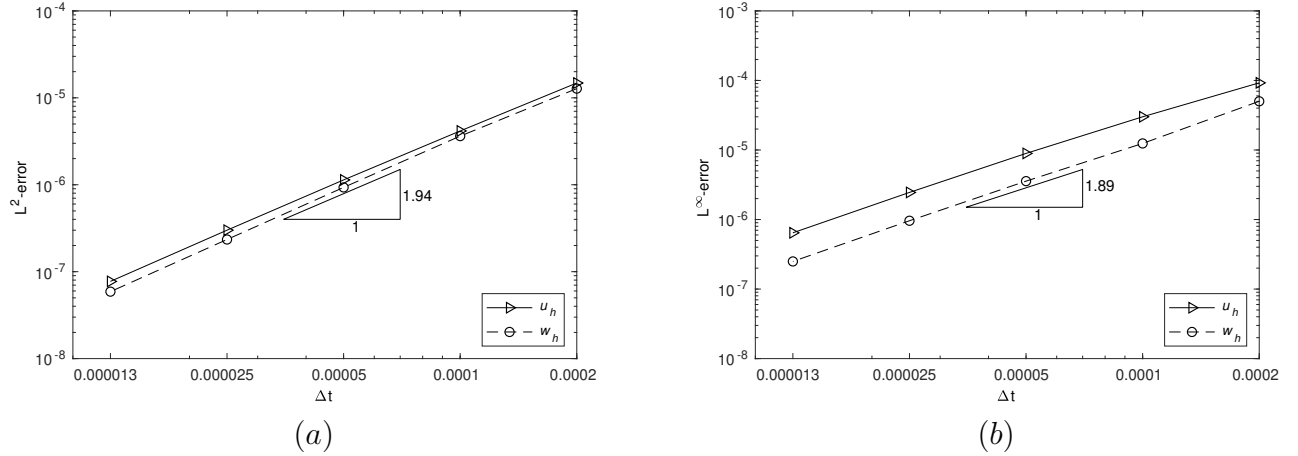


Figure 3: Temporal convergence rate: (a) L^2 -error, and (b) L^∞ -error on \hat{u}_h and \hat{w}_h , respectively, as function of time step size Δt . Results are obtained with \mathbb{P}_2 elements and Dirichlet conditions.

4.1.2. Analytic solution

In the previous subsection, optimal convergence rates have been obtained for constant mobility function. It is the main purpose of this subsection to numerically study the convergence rates for non-constant mobility function by using a particular analytic solution.

Setting $f(u) = u$, $\varphi = 0$ and $\gamma = 1$ in (2.2), we get the nonlinear fourth-order equation

$$u_t + \nabla \cdot (u \nabla \Delta u) = 0 \quad \text{in } \Omega \times (0, T). \quad (4.7)$$

Equation (4.7) has a nonnegative closed-form compactly-supported, 2-dimensional self-similar solution [26] given by

$$u(x, y, t) = \begin{cases} \frac{t^{-1/3}}{192} (L^2 - r^2)^2, & r < L, \\ 0, & r \geq L, \end{cases} \quad r = \frac{\sqrt{x^2 + y^2}}{t^{1/6}}. \quad (4.8)$$

In the framework of the mixed formulation, we need the auxiliary variable $w = -\Delta u$, which is calculated in a straightforward way from (4.8) to get

$$w(x, y, t) = \begin{cases} \frac{t^{-2/3}}{24} (L^2 - 2r^2), & r < L, \\ 0, & r \geq L. \end{cases} \quad (4.9)$$

The auxiliary variable (4.9) is not continuous at point where $r = L$. Moreover, the source-type solution (4.8) tends to a Dirac mass as t goes to zero. Therefore, we have to choose L large enough and a starting time $t_0 > 0$ to ensure the regularity of the solution (4.8)-(4.9) for the mixed formulation. Here, there is no energy term, but the mobility function depends on the solution. This will allow to test the impact of the numerical treatment for the mobility function, based on extrapolation.

To test the spatial convergence rates, we compute the L^2 - and H^1 -error norms between the exact solution (4.8)-(4.9) and the numerical solution computed with the proposed method (3.6)-(3.7), where we set $\varphi \equiv 0$. We use the same computational domain, meshes, finite element approximations as in section 4.1.1. Since, we focus on the spatial convergence rates, we use a small time step $\Delta t = 10^{-8}$ to minimize the temporal error from the extrapolation of the non constant mobility. We choose $L = 3$ and a starting time $t_0 = 0.001$. Tables 1 and 2 show the computational time, the L^2 - and H^1 -error as function of the element h , computed with Dirichlet and Neumann boundary conditions, respectively. The formula to obtain the order of convergence in space, p , reads:

$$p = \ln \left(\frac{\|u - u_h\|}{\|u - u_{h/\tau}\|} \right) / \ln \tau, \quad (4.10)$$

where $\tau > 0$ is the refinement factor between consecutive element sizes. The value $\tau = 2$ was chosen in our numerical experiments. By using the formula (4.10), we get from Table 1 that the convergence rates in the H^1 -norm are about 1 and 2 for the linear and quadratic Lagrange elements, respectively, while the convergence rates in the L^2 -norm are approximately 2 and 4 for the linear and quadratic Lagrange elements, respectively. These same convergence rates were obtained with a manufactured solution in section 4.1.1 (see Figure 1). Formula (4.10), used on Table 2, gives approximately the same rates of convergence as in Figure 2 (for Neumann boundary conditions). While the quadratic Lagrange elements provide smaller error than the linear Lagrange elements, they are also the most computationally expensive. However, the quadratic Lagrange elements with mesh size $2h$ provide superior accuracy than the linear elements with mesh size h , and both require

approximately the same computational cost. Therefore, high-order finite element approximations are beneficial in terms of efficiency. We also have computed the L^2 - and H^1 -error on the auxiliary w_h and have found the same orders of convergence as for u_h , except in the H^1 -error for quadratic Lagrange elements, which leads to super-convergence of order $\mathcal{O}(h^3)$.

Mesh	Linear Lagrange elements			Quadratic Lagrange elements		
	L^2 -error	H^1 -error	CPU (s)	L^2 -error	H^1 -error	CPU (s)
25×25	14.4303×10^{-6}	0.223426	15.80	599.199×10^{-9}	41.7231×10^{-4}	25.98
50×50	3.64952×10^{-6}	0.111751	25.99	37.8744×10^{-9}	10.4412×10^{-4}	63.63
100×100	0.91474×10^{-6}	0.055880	63.36	2.37924×10^{-9}	2.61096×10^{-4}	221.69
200×200	0.22881×10^{-6}	0.027940	222.52	0.14958×10^{-9}	0.65278×10^{-4}	971.67

Table 1: CPU time, L^2 - and H^1 -error as a function of the element size h , computed with linear and quadratic Lagrange elements, respectively. Results are obtained with Dirichlet boundary conditions.

Mesh	Linear Lagrange elements			Quadratic Lagrange elements		
	L^2 -error	H^1 -error	CPU (s)	L^2 -error	H^1 -error	CPU (s)
25×25	204.486×10^{-6}	0.223103	16.10	3799.57×10^{-9}	41.0548×10^{-4}	27.01
50×50	51.5883×10^{-6}	0.111696	26.21	336.114×10^{-9}	10.3552×10^{-4}	64.37
100×100	12.9592×10^{-6}	0.055871	63.97	29.7100×10^{-9}	2.60006×10^{-4}	223.69
200×200	3.24528×10^{-6}	0.027939	224.72	2.62640×10^{-9}	0.65140×10^{-4}	992.07

Table 2: CPU time, L^2 - and H^1 -error as a function of the element size h , computed with linear and quadratic Lagrange elements, respectively. Results are obtained with Neumann boundary conditions.

For the error and convergence analysis in time, we compute a reference solution $(u_h^{\text{ref}}, w_h^{\text{ref}})$ on a grid of 100×100 using linear Lagrange elements and a time step $\Delta t = 10^{-5}$. We then analyze the numerical convergence in time by varying the time step Δt systematically between 0.001 and 0.008. For each time step, the errors on u_h and w_h , computed as

$$\frac{\|u_h^{\text{ref}} - u_h\|_{L^2(\Omega)}}{\|u_h^{\text{ref}}\|_{L^2(\Omega)}} \quad \text{and} \quad \frac{\|w_h^{\text{ref}} - w_h\|_{L^2(\Omega)}}{\|u_h^{\text{ref}}\|_{L^2(\Omega)}}, \quad (4.11)$$

respectively, are recorded at the final time $T = 0.201$. Table 3 shows the error, computational time and order of convergence of the numerical solution with respect to the reference solution. The rate of convergence in time is calculated using the formula (4.10), where τ is the refinement factor between consecutive time steps. Here, also $\tau = 2$ was chosen in our numerical tests. A second-order convergence rate in time is obtained.

4.2. Numerical results — Applications

4.2.1. Lubrication

Equation (4.7) appears in the lubrication approximation of a thin viscous film, which is driven by surface tension. In this context, u describes the height of the liquid film which spreads on a solid surface [29, 34]. The numerical solutions of high-order nonlinear degenerate diffusion equations like (4.7) require special numerical techniques in order to preserve the non-negativity of solutions. Constructing finite element methods that guarantee the non-negativity of the solutions of (4.7), has been initiated by Barrett et al. [3] by enforcing at each time step the non-negativity of the

Δt	Relative L^2 -error		Order of convergence		CPU (s)
	Error on u_h	Error on w_h	Order for u_h	Order for w_h	
0.008	1.4340×10^{-6}	3.4856×10^{-5}	2.079	2.079	50.367
0.004	3.3927×10^{-7}	8.2465×10^{-6}	2.038	2.038	95.467
0.002	8.2570×10^{-8}	2.0070×10^{-6}	2.019	2.019	190.636
0.001	2.0369×10^{-8}	4.9512×10^{-7}	—	—	386.169

Table 3: Relative L^2 -error as a function of time step Δt , order of convergence (in time) and CPU time. Results are obtained with Dirichlet boundary conditions.

approximate solution as a constraint, which leads to a variational inequality. The solutions of the one-dimensional version of (4.7) using a non-negativity preserving scheme was carried out in [30]. The solution of a modified problem, which consists in approximating the mobility term $f(u) = u$ by

$$f_\xi(u) = \frac{u^5}{\xi u + u^4}, \quad (4.12)$$

has been shown by [6] to remain positive. This regularization is used in [8, 50] to compute numerical solutions of (4.7) for the initial data

$$u(x, y, 0) = \delta + Ce^{-\sigma(x^2+y^2)}, \quad (4.13)$$

where $\delta > 0$ represents the thickness of an ultra-thin precursor film under the Gaussian fluid droplet centered at the origin. Here, we solve (4.7) without regularization, i.e. with the degenerate mobility function $f(u) = u$. The computational domain is the rectangle $[-0.5, 0.5] \times [-1, 1]$. Homogeneous Neumann conditions (2.4) are imposed on the boundary. We use linear Lagrange elements on a uniform mesh 70×140 , i.e. a mesh size $h = 0.02$. We set $\delta = 0.01$, $\sigma = 80$ and $C = 2$. The same values for these parameters and mesh size were used in [8]. The contours of the numerical solutions and a 3D view of the droplet at different times are shown in Figure 4. The algorithm (3.6)-(3.7) preserves the positivity of the solution up to a maximal time step of $\Delta t \simeq 10^{-5}$. We have also performed numerical simulations for $C = 1$ as in [50], for which the positivity has been preserved up to a maximal time step of $\Delta t \simeq 0.01$, while $\Delta t = 10^{-5}$ was found in [50] as the maximal time step to preserve the positivity.

To show that the numerical scheme satisfies the energy decreasing property (2.7), we define the discrete energy functional of (4.7) as

$$\varepsilon_h(u_h^n) = \frac{1}{2} \int_{\Omega} |\nabla u_h^n|^2 d\mathbf{x}, \quad (4.14)$$

and consider the evolution of the discrete energy. Figure 5(a) shows the time-evolution of the discrete total energy. Our results demonstrate that the total discrete energy is non-increasing which agrees well with the total energy dissipation property.

The maximum of the solution of (4.7) with the initial condition (4.13) occurs at the origin for all times. Figure 5(b) shows the height of the droplet at the origin as time evolves. After an initial transient phase ($t > 10^{-5}$), the maximal height $u(0, t)$ evolves in $t^{-1/3}$ for some times, and in $t^{-1/5}$ for longer times, before approaching a uniform flat state for large times ($t > 10^{-1}$). The same evolutions are observed in [8, 50].

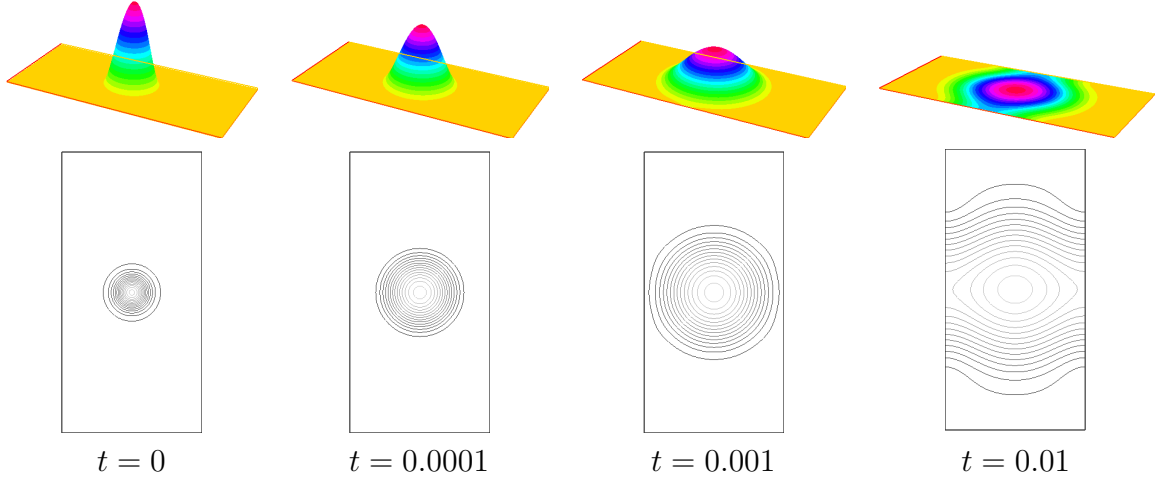


Figure 4: Numerical solution of (4.7) starting from (4.13). Top: A 3D view of the droplet spreading on a solid surface. Bottom: Contours at various times of the simulated solution. $\Delta t = 10^{-5}$.

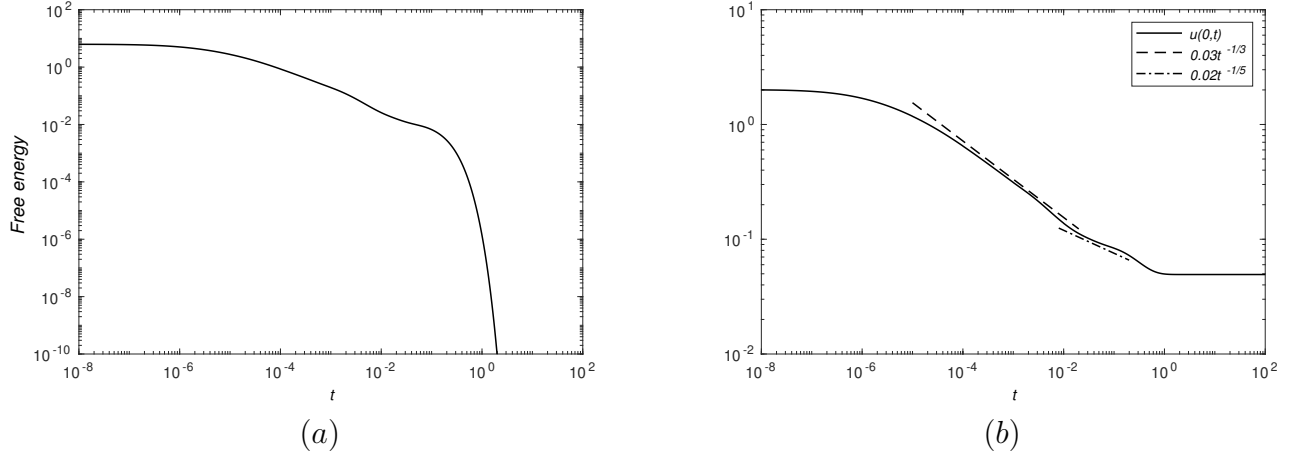


Figure 5: (a) Monotonic decrease of the total free energy estimate. (b) Evolution of the droplet maximal height $u(0,t)$ showing the intermediate asymptotics.

4.2.2. Phase separation

Spinodal decomposition is a mechanism by which a solution of two or more components can separate into distinct phases. Spinodal decomposition in a binary mixture is well-described by the Cahn-Hilliard equation [11, 12]. Here, we are interested in the phase separation of a homogeneous binary mixture governed by (2.2) to further test our method (3.6)-(3.7). As in [48], we choose a mobility function $f(u) = (1 - u^2)$, a free energy function $\varphi(u) = \frac{1}{4\epsilon^2}(u^2 - 1)^2$ and set the parameters $\gamma = 1$ and $\epsilon = 0.03$. In this case, equation (2.2) describes the state of a relative concentration $u = (2\frac{u_a}{u_a + u_b} - 1)$, where u_a and u_b are the concentrations of the two components [27]. With this double well form of the energy function, the system is locally in one of the two phases if u is close to one of the two minima ± 1 of φ [22].

The initial condition is chosen as

$$u_0(\mathbf{x}) = \bar{u} + \sum_{i=1}^M c_i r_i(\mathbf{x}, \mathbf{a}_i), \quad (4.15)$$

where $\bar{u} \in [-1, 1]$, $\mathbf{a}_i \in \mathbb{R}^2$, $c_i \in \mathbb{R}$, for $i = 1, \dots, M$, and $r_i(\mathbf{x}, \mathbf{a}_i) = e^{-1000|\mathbf{x}-\mathbf{a}_i|^2}$. We have randomly generated $M = 1000$ points \mathbf{a}_i in the square domain $[0, 1] \times [0, 1]$, and 1000 scalars $c_i \in [-0.01, 0.01]$. All numerical results in this section are computed on a 64×64 grid with quadratic Lagrange elements. Figure 6 shows the initial condition for two different values of \bar{u} .

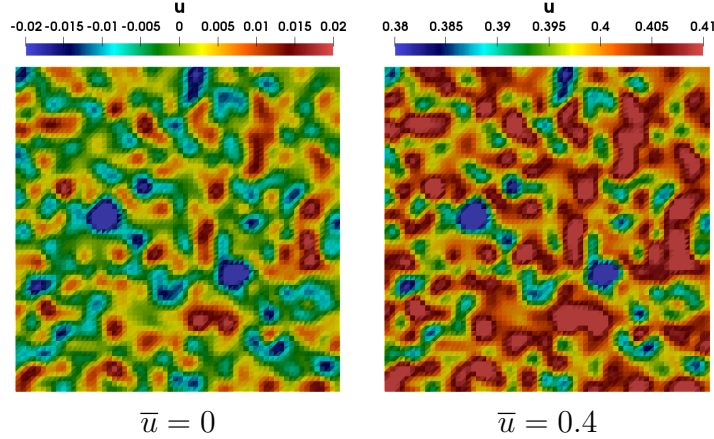


Figure 6: Initial solution for different values of \bar{u} .

We first consider the initial solution for $\bar{u} = 0$. The dynamics of the binary fluid are shown in Figure 7. From its initial concentration, the system separates quickly into two phases whose composition is determined by the two minima ± 1 of the free energy function. Small regions of the same phase combine together to form larger patterns, reducing the interface boundaries between the two phases.

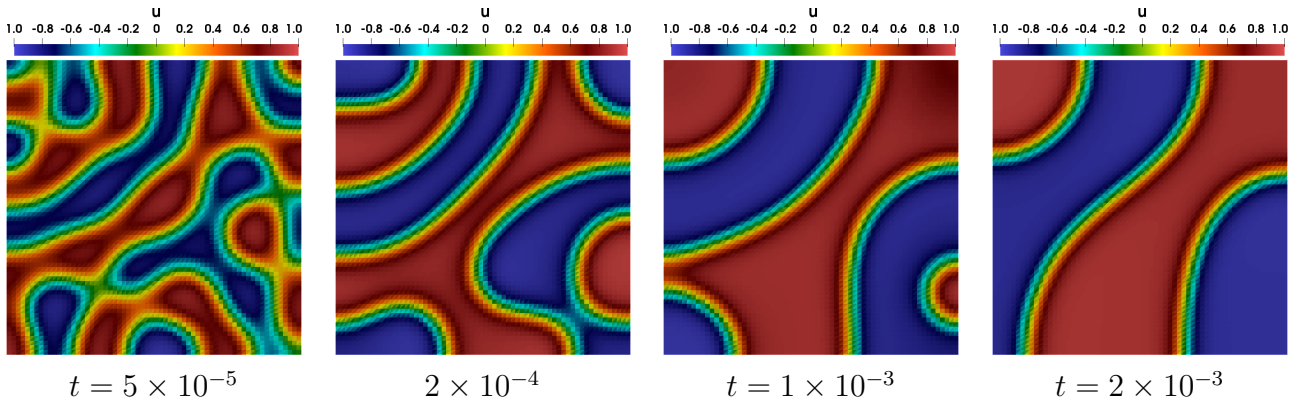


Figure 7: Simulation of a spinodal decomposition starting from a uniformly distributed random initial condition. $\Delta t = 10^{-6}$.

A particular regime of interest is when one phase is significantly more abundant in the initial mixture. In such case, the minority phase emerges and forms droplets. Larger particles grow at

the expense of the smaller ones which shrink and disappear. This form of competitive growth is known as the Ostwald ripening [43]. To illustrate such regime, we use the initial solution for $\bar{u} = 0.4$. Figure 8 shows the time-evolution of the binary mixture computed. We can observe the formation of droplets. Smaller droplets are absorbed into larger ones through diffusion, exhibiting clearly the phenomenon of Ostwald ripening.

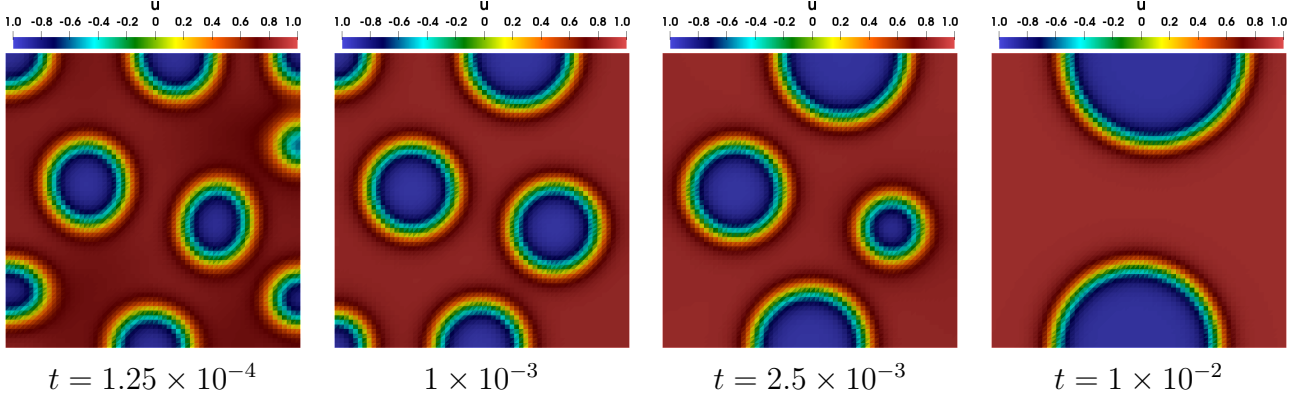


Figure 8: Simulation of a Ostwald ripening process starting from a perturbation of an uniform state. $\Delta t = 10^{-6}$.

We qualitatively observe the same behavior of the solution as in [48]. The plots of the energy evolution in Figure 9 illustrates that the total discrete energy satisfies the energy dissipation property. Plots of the discrete total mass are shown in Figure 10, which illustrate the mass-conservative property of the linear scheme. We observe that the magnitude and the nonlinearity of the mobility have a significant direct impact on the stability of the scheme. We have noticed from numerical experiments that a small time step is required for the stability of numerical solutions involving non constant mobility functions. The time step could be taken larger for constant mobility functions and regular energy functions. The parameter γ has an impact on the length scale of the diffuse interface by balancing the surface energy term with the bulk free energy [7]. In terms of the stability of the scheme, there is a strong link between the parameter γ and the free energy term.

4.2.3. Electrowetting

Electrowetting has become one of the most widely used tools for manipulating tiny amounts of liquids on surfaces. It consists in the modification of the wetting properties of a surface with an applied electric field. A diffuse-interface model for drop motion, due to electrowetting, in a Hele-Shaw geometry is proposed in [41]. The model is governed by the Cahn-Hilliard model with a spatially dependent energy

$$\begin{cases} \epsilon u_t - \nabla \cdot (u \nabla w) = 0, \\ w = -\epsilon^2 \Delta u + \varphi'(u) - \epsilon \rho(\mathbf{x}), \end{cases} \quad (4.16)$$

with a double well energy function $\varphi(u) = (u - \epsilon)^2(u - 1)^2$, where $\rho(\mathbf{x}) = \lambda \chi(\mathbf{x})$ defines a local energy (electric field) with characteristic function $\chi(\mathbf{x})$ and strength λ . The local energy term introduces the electrowetting into the diffuse-interface model. The parameter $\epsilon = 0.0427$ controls the diffuse interface thickness. For more details and the experimental setup, we refer to [41].

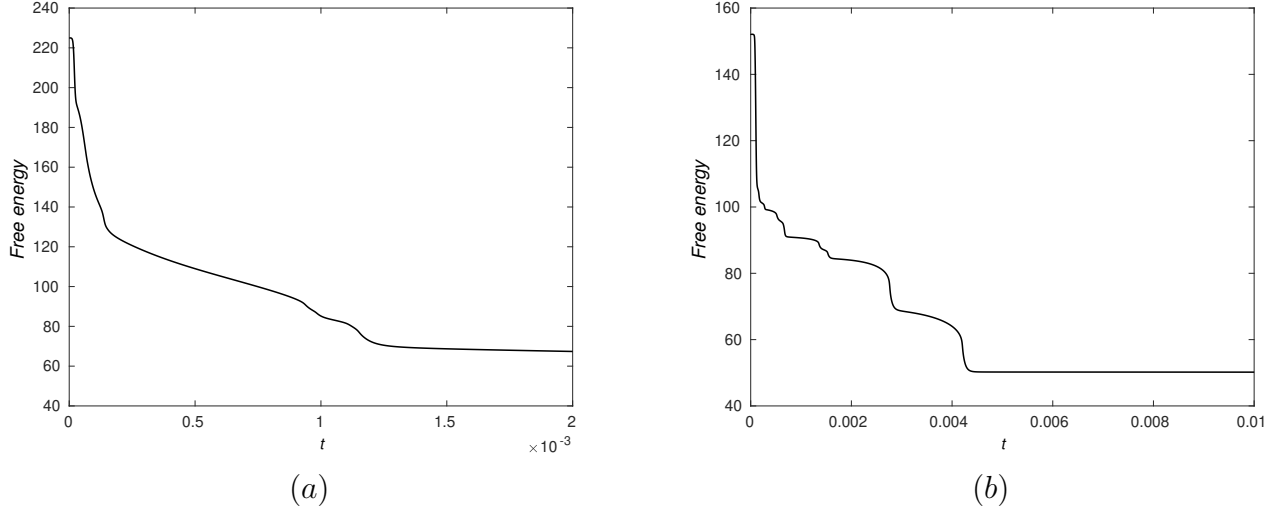


Figure 9: Free energy evolutions. (a) for the spinodal decomposition and (b) for the Ostwald ripening.

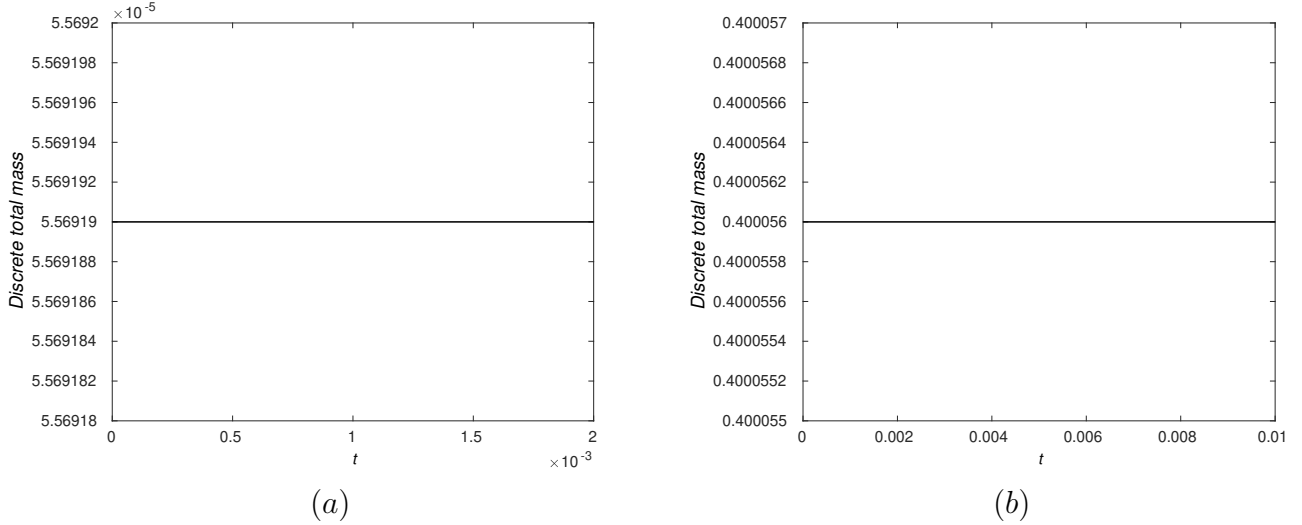


Figure 10: Numerical verification of the total mass conservation over time. (a) for the spinodal decomposition and (b) for the Ostwald ripening.

We solve this problem using a Gaussian initial data

$$u_0(\mathbf{x}) = \delta + e^{-10|\mathbf{x}-\mathbf{a}|^2}, \quad (4.17)$$

representing a droplet centered at the point \mathbf{a} that will be specified for each test case. All numerical results in this section are computed on a 47×94 grid in the rectangular domain $[-0.5, 0.5] \times [-1, 1]$ using linear Lagrange elements. This gives rise to a mesh size $h \approx 0.03$ as in [8, 41]. We use a precursor film $\delta = \epsilon$ and a fixed time step $\Delta t = 0.001$ instead of adaptative time steps as in [8].

We first consider a droplet centered at point $\mathbf{a} = (0, -0.3)$ and then apply the electric field $\rho(\mathbf{x})$ on the surface $y > 0$. The time-evolution of the droplet is displayed in Figure 11. The

surface of the droplet is deformed during its translation toward the region with low energy (with an electric field). The variation of the curvature of the droplet increases with the strength λ of the electric field. The same evolutions are observed using numerical simulations in [8, 41] and experimentally in [41].

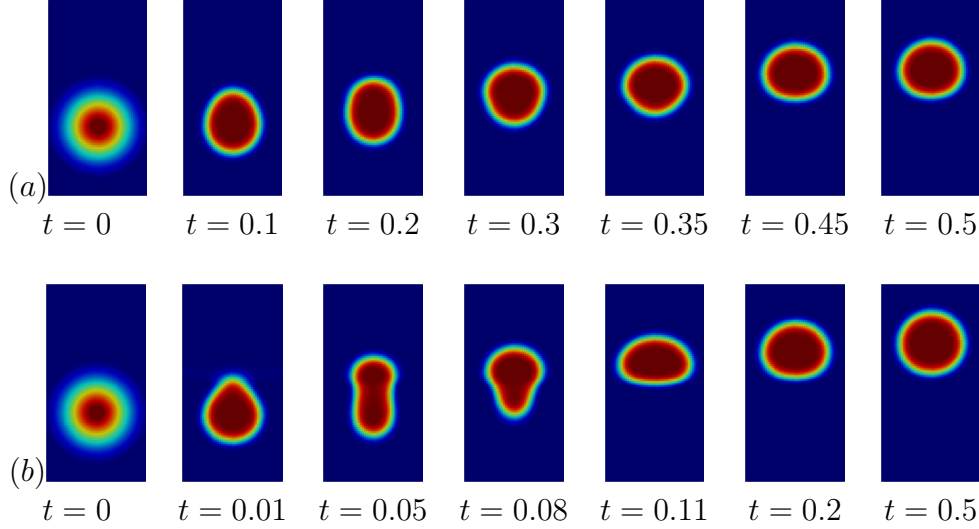


Figure 11: Droplet translation by electrowetting: (a) solution for $\lambda = 0.75$ and (b) $\lambda = 3$. $\Delta t = 10^{-3}$.

We next consider a droplet centered at the origin $\mathbf{a} = (0, 0)$ and apply two electric fields of same strength $\lambda = 2$ on the surfaces $y < -0.3$ and $y > 0.3$, respectively. For this test case, we also want to compare the time it takes for a nonlinear scheme, namely the second-order backward differentiation formula (BDF2), and for the linear scheme introduced in our study. The BDF2 scheme is second-order accurate in time and consists in approximating the temporal derivative as in (3.6) and treating all other terms implicitly. This fully implicit method uses an iterative procedure to solve the nonlinear resulting system. Here, we use Newton method with a tolerance of 10^{-6} for the iterative solver. Numerical results for both methods are displayed in Figure 12, which shows the capability of the proposed method to simulate the macroscopic dynamics of drop splitting as with the nonlinear BDF2 scheme but with a relatively smaller computational time. In fact, we can see from Table 4 that the algorithm (3.6)-(3.7) is in average four times faster than the BDF2 scheme. Though the maximal time step for the proposed scheme can be smaller than for BDF methods, the required CPU time is still significantly smaller than with BDF methods.

Final time t_f	CPU (s)	
	Algorithm (3.6)-(3.7)	BDF2 scheme
0.018	4.48	17.78
0.036	8.36	34.51
0.072	16.88	66.58
0.144	33.00	137.66

Table 4: Computation time comparison between the algorithm (3.6)-(3.7) and the BDF2 scheme for the droplet splitting test case. $\Delta t = 10^{-3}$, $\lambda = 2$.

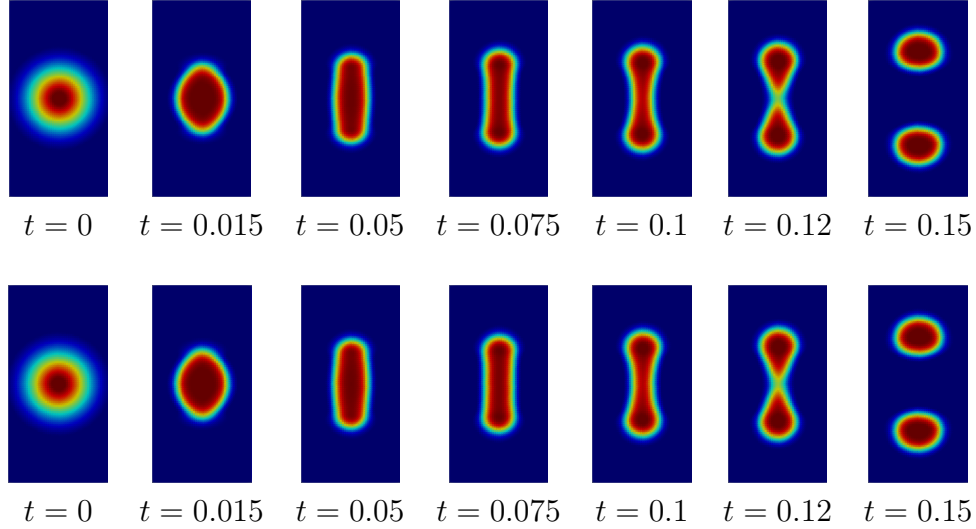


Figure 12: Droplet splitting by electrowetting: (top) solution with the algorithm (3.6)-(3.7) and (bottom) solution with BDF2 scheme. $\Delta t = 10^{-3}$, $\lambda = 2$.

5. Conclusion

The present study provides a new fully discrete mixed finite element method to approximate fourth-order nonlinear diffusion equations. We develop a special numerical technique of approximating the nonlinear energy term that allows to design a linear scheme for our system. The performance of our scheme is tested using relevant numerical examples, and the results clearly demonstrated the ability of the proposed scheme to resolve fourth-order nonlinear diffusion equations. Manufactured and analytic solutions have been used for the numerical investigation of the accuracy of the scheme. We have performed numerical analysis and presented convergence results showing the good behavior of the numerical method with respect to mesh refinement, order of the approximation and boundary conditions. With respect to the spatial discretization, convergence rates are obtained that match analytical error estimates available for linear problems. We also have presented a series of numerical experiments to confirm the second-order accuracy in time for both constant and non-constant mobility function. Some complex and real-world examples are presented including a model for electrowetting on dielectric and for coarsening dynamics of binary mixture.

Acknowledgement

The first and second authors are supported by the UM6P/OCP group of Morocco. The third author is supported through a Discovery Grant of the Natural Sciences and Engineering Research Council of Canada.

References

References

- [1] F. Amiri, D. Millán, M. Arroyo, M. Silani, and T. Rabczuk. Fourth order phase-field model for local max-ent approximants applied to crack propagation. *Comput. Methods Appl. Mech.*

Eng., 312:254–275, 2016.

- [2] J. Barrett and J. Blowey. Finite element approximation of the Cahn-Hilliard equation with concentration dependent mobility. *Math. Comp.*, 68:286–318, 1999.
- [3] J. Barrett, J. Blowey, and H. Garcke. Finite element approximation of a fourth order nonlinear degenerate parabolic equation. *Numer. Math.*, 80:525–556, 1998.
- [4] J. Barrett, J. Blowey, and H. Garcke. Finite element approximation of the Cahn-Hilliard equation with degenerate mobility. *SIAM J. Num. Anal.*, 37:286–318, 1999.
- [5] A. Beljadid, L. Cueto-Felgueroso, and R. Juanes. A continuum model of unstable infiltration in porous media endowed with an entropy function. *Adv. Water Resour.*, 144:103684, 2020.
- [6] F. Bernis and A. Friedman. Higher order nonlinear degenerate parabolic equations. *J. Differ. Equ.*, 83:179–206, 1990.
- [7] A. L. Bertozzi, S. Esedoglu, and A. Gillette. Inpainting of binary images using the Cahn-Hilliard equation. *IEEE Trans. Image Process.*, 16:285–291, 2007.
- [8] A. L. Bertozzi, N. Ju, and H.-W. Lu. A biharmonic-modified forward time stepping method for fourth order nonlinear diffusion equations. *Discrete Contin. Dyn. Syst. A*, 29:1367–1391, 2011.
- [9] D. Boffi, F. Brezzi, and M. Fortin. *Mixed Finite Element Methods and Applications*. Springer-Verlag Berlin Heidelberg, 2013.
- [10] S. Brenner, S. Gu, T. Gudi, and L. Sung. A quadratic C0 interior penalty method for linear fourth order boundary value problems with boundary conditions of the Cahn-Hilliard type. *SIAM J. Numer. Anal.*, 50:2088–2110, 2012.
- [11] J. W. Cahn. On spinodal decomposition in cubic crystals. *Acta Metall.*, 10:179–183, 1962.
- [12] J. W. Cahn and J. E. Hilliard. Free energy of a nonuniform system. I. Interfacial free energy. *J. Chem. Phys.*, 28:258–267, 1958.
- [13] P. Colli, G. Gilardi, E. Rocca, and J. Sprekels. Optimal distributed control of a diffuse interface model of tumor growth. *Nonlinearity*, 30:2518–2546, 2017.
- [14] L. Cueto-Felgueroso and R. Juanes. A phase field model of unsaturated flow. *Water Resour. Res.*, 45:W10409, 2009.
- [15] S. Dai and Q. Du. Weak solutions for the Cahn-Hilliard equation with degenerate mobility. *Arch. Ration. Mech. Anal.*, 219:1161–1184, 2016.
- [16] S. Dargaville and T. W. Farrell. A least squares based finite volume method for the Cahn-Hilliard and Cahn-Hilliard-reaction equations. *J. Comput. Appl. Math.*, 273:225–244, 2015.
- [17] T. A. Davis. Algorithm 832: UMFPACK — an unsymmetric-pattern multifrontal method. *ACM Trans. Math. Softw.*, 30:196–199, 2004.

- [18] É. J. M. Delhez and É. Deleersnijder. Overshootings and spurious oscillations caused by biharmonic mixing. *Ocean Model.*, 17:183–198, 2007.
- [19] Q. Du, L. Ju, and L. Tian. Finite element approximation of the Cahn-Hilliard equation on surfaces. *Comput. Methods Appl. Mech. Eng.*, 200:2458–2470, 2011.
- [20] G. Dziuk and C. M. Elliott. Eulerian finite element method for parabolic PDEs on implicit surfaces. *Interfaces Free Bound.*, 10:119–138, 01 2008.
- [21] P. Ehrhard and S. H. Davis. Non-isothermal spreading of liquid drops on horizontal plates. *J. Fluid Mech.*, 229:365–388, 1991.
- [22] C. M. Elliott. The Cahn-Hilliard Model for the Kinetics of Phase Separation. In J. F. Rodrigues, editor, *Mathematical Models for Phase Change Problems*, volume 88, pages 35–73. Birkhäuser Basel, 1989.
- [23] C. M. Elliott, D. A. French, and F. A. Milner. A second order splitting method for the Cahn-Hilliard equation. *Numer. Math.*, 54:575–590, 1989.
- [24] C. M. Elliott and H. Garcke. On the Cahn-Hilliard equation with degenerate mobility. *SIAM J. Math. Anal.*, 27:404–423, 1996.
- [25] E. L. Elson, E. Fried, J. E. Dolbow, and G. M. Genin. Phase separation in biological membranes: integration of theory and experiment. *Annu. Rev. Biophys.*, 39:207–226, 2010.
- [26] R. Ferreira and F. Bernis. Source-type solutions to thin-film equations in higher dimensions. *Euro. J. Appl. Math.*, 8:507–524, 1997.
- [27] H. Garcke, B. Niethammer, R. Rumpf, and U. Weikard. Transient coarsening behaviour in the Cahn-Hilliard model. *Acta Mater.*, 51:2823–2830, 2003.
- [28] L. Goudenège, D. Martin, and G. Vial. High order finite element calculations for the Cahn-Hilliard equation. *J. Sci. Comput.*, 52:294–321, 2012.
- [29] H. P. Greenspan. On the motion of a small viscous droplet that wets a surface. *J. Fluid Mech.*, 84:125–143, 1978.
- [30] G. Grün and M. Rumpf. Nonnegativity preserving convergent schemes for the thin film equation. *Numer. Math.*, 87:113–152, 2000.
- [31] F. Guillén-González and G. Tierra. On linear schemes for a Cahn-Hilliard diffuse interface model. *J. Comput. Phys.*, 234:140–171, 2013.
- [32] L.-P. He and Y. Liu. A class of stable spectral methods for the Cahn-Hilliard equation. *J. Comput. Phys.*, 228:5101–5110, 2009.
- [33] F. Hecht. New development in FreeFem++. *J. Numer. Math.*, 20:251–265, 2012.
- [34] L. M. Hocking. Sliding and spreading of thin two-dimensional drops. *Quart. J. Mech. Appl. Math.*, 34:37–55, 1981.

- [35] H. E. Huppert. Flow and instability of a viscous current down a slope. *Nature*, 300:427–429, 1982.
- [36] A. M. Jokisaari, P. W. Voorhees, J. E. Guyer, J. Warren, and O.G. Heinonen. Benchmark problems for numerical implementations of phase field models. *Comput. Mater. Sci*, 126:139–151, 2017.
- [37] S. Kaessmair and P. Steinmann. Comparative computational analysis of the Cahn-Hilliard equation with emphasis on C1-continuous methods. *J. Comput. Phys.*, 322:783–803, 2016.
- [38] M. Kästner, P. Metsch, and R. de Borst. Isogeometric analysis of the Cahn-Hilliard equation — a convergence study. *J. Comput. Phys.*, 305:360–371, 2016.
- [39] E. Khain and L. Sander. Generalized Cahn-Hilliard equation for biological applications. *Phys. Rev. E Stat. Nonlin. Soft Matter Phys.*, 77:051129, 2008.
- [40] J. S. Lowengrub, H. B. Frieboes, F. Jin, Y.-L. Chuang, X. Li, P. Macklin, S. M. Wise, and V. Cristini. Nonlinear modelling of cancer: bridging the gap between cells and tumours. *Nonlinearity*, 23:R1–R91, 2010.
- [41] H.-W. Lu, K. Glasner, A. L. Bertozzi, and C.-J. Kim. A diffuse-interface model for electrowetting drops in a Hele-Shaw cell. *J. Fluid Mech.*, 590:411–435, 2007.
- [42] J. A. Moriarty, L. W. Schwartz, and E. O. Tuck. Unsteady spreading of thin liquid films with small surface tension. *Phys. Fluids A*, 3:733–742, 1991.
- [43] L. M. Pismen. *Patterns and Interfaces in Dissipative Dynamics*. Springer-Verlag Berlin Heidelberg, 2006.
- [44] D. Qiang and R. A. Nicolaides. Numerical analysis of a continuum model of phase transition. *SIAM J. Numer. Anal.*, 28:1310–1322, 1991.
- [45] H. H. Rosenbrock. Some general implicit processes for the numerical solution of differential equations. *Comput. J.*, 5:329–330, 1963.
- [46] J. Shen and X. Yang. Numerical approximations of Allen-Cahn and Cahn-Hilliard equations. *Discrete Contin. Dyn. Syst. A*, 28:1669–1691, 2010.
- [47] J. Shin, D. Jeong, and J. Kim. A conservative numerical method for the Cahn-Hilliard equation in complex domains. *J. Comput. Phys.*, 230(19):7441–7455, 2011.
- [48] P. Vignal, N. Collier, L. Dalcin, D. L. Brown, and V. M. Calo. An energy-stable time-integrator for phase-field models. *Comput. Methods Appl. Mech. Eng.*, 316:1179–1214, 2017.
- [49] S. M. Wise, J. S. Lowengrub, H. B. Frieboes, and V. Cristini. Three-dimensional multispecies nonlinear tumor growth—I Model and numerical method. *J. Theor. Biol.*, 253:524–543, 2008.
- [50] T.P. Witelski and M. Bowen. ADI schemes for higher-order nonlinear diffusion equations. *Appl. Numer. Math.*, 45:331–351, 2003.

- [51] X. Wu, G. J. van Zwieten, and K. G. van der Zee. Stabilized second-order convex splitting schemes for Cahn-Hilliard models with application to diffuse-interface tumor-growth models. *Int. J. Numer. Meth. Biomed. Engng.*, 30:180–203, 2014.
- [52] Z. Yang, L. Lin, and S. Dong. A family of second-order energy-stable schemes for Cahn-Hilliard type equations. *J. Comput. Phys.*, 383:24–54, 2019.
- [53] X. Ye and X. Cheng. The Fourier spectral method for the Cahn-Hilliard equation. *Appl. Math. Comput.*, 171:345–357, 2005.
- [54] L. Zhang, M. R. Tonks, D. Gaston, J. W. Peterson, D. Andrs, P. C. Millett, and B. S. Biner. A quantitative comparison between C0 and C1 elements for solving the Cahn-Hilliard equation. *J. Comput. Phys.*, 236:74–80, 2013.
- [55] L. Zhornitskaya and A. L. Bertozzi. Positivity-preserving numerical schemes for lubrication-type equations. *SIAM J. Numer. Anal.*, 37:523–555, 1999.